frontiers | Frontiers in Earth Science

TYPE Original Research
PUBLISHED 05 September 2025
DOI 10.3389/feart.2025.1639022

OPEN ACCESS

EDITED BY
Stanislaw Mazur,
Polish Academy of Sciences, Poland

REVIEWED BY
Tong Hou,
China University of Geosciences, China
Liang Qiu,
China University of Geosciences, China

*CORRESPONDENCE
Hongqi Yuan,
yuanhongqi@nepu.edu.cn

RECEIVED 01 June 2025
ACCEPTED 15 August 2025
PUBLISHED 05 September 2025

CITATION
Li J, Wang Q, Li M, Jiang S, Han J, Guan L, Yu Y and Yuan H (2025) Geochemistry, geochronology, and tectonic significance of diorite porphyry from the Northern Daheishan Horst in NE China.
Front. Earth Sci. 13:1639022.
doi: 10.3389/feart.2025.1639022

Geochemistry, geochronology, and tectonic significance of diorite porphyry from the Northern Daheishan Horst in NE China

Jie Li[1], Qi Wang[1], Mengxia Li[1], Shan Jiang[1], Jing Han[1], LinXuan Guan[2], Yinghua Yu[2] and Hongqi Yuan[2]*

[1]Exploration and Development Research Institute of PetroChina Daqing Oilfield Company Limited, Daqing, China, [2]School of Earth Sciences, Northeast Petroleum University, Daqing, China

The Daheishan Horst is located in the eastern segment of the Solonker-Xar Moron River-Changchun-Yanji Suture (SXCYS), between the eastern margin of the Songliao Basin and the Jiayi Fault Zone. The Daheishan Horst serves as a critical area for studying the evolutionary processes of the eastern Paleo-Asian Ocean (PAO). Current debates persist regarding the formation age, tectonic setting, and evolution of magmatic rocks in the Daheishan Horst. To address these controversies, this study examines diorite porphyry dikes exposed in Heibei Village, Jilin City, Jilin Province, through comprehensive analyses including: whole-rock major, trace, and rare earth elements; zircon U-Pb dating; zircon Hf isotopes; and whole-rock Sr-Nd isotopes. These investigations aim to determine the formation age and tectonic evolution of the magmatic rocks in the Daheishan Horst. Key findings include: (1) Zircon U-Pb ages (252.9 $\pm$ 3.2 Ma) indicate Late Permian emplacement; (2) The magmatic rocks are predominantly subalkaline and belong to the medium-K calc-alkaline series. They exhibit enrichment in large-ion lithophile elements (LILEs) and light rare earth elements (LREEs), with significant depletion in high-field-strength elements (HFSEs: Nb, Ta, P, Ti), consistent with arc-type or active continental margin magmatism; (3) Zircon Hf and whole-rock Sr-Nd isotopic analyses indicate magma derivation primarily from partial melting of depleted mantle sources, with negligible contamination from ancient crustal materials; (4) Geochemical signatures include positive La/Sm-La correlations, elevated Th contents (6.21–11.66 ppm), Th/Yb = 2.52–3.66, Zr/Y = 9.7–11.5, and Ta/Yb = 0.12–0.28. These features are diagnostic of oceanic-continental subduction zone magmatism, confirming origination from partial melting of subduction-fluid-metasomatized mantle. This study concludes that the magmatic rocks of the Daheishan Horst formed during subduction beneath an active continental margin. Our results reveal a bidirectional subduction with scissor-like closure model along the SXCYS in the eastern Paleo-Asian Ocean, with closure propagating westward to eastward from the Late Permian to Early/Middle Triassic.

KEYWORDS

Daheishan horst, Jilin Province, zircon U-Pb dating, geochemistry, EasternSegment of the Paleo-Asian ocean

1 Introduction

The Daheishan Horst, located in central Jilin Province, represents a Mesozoic-Cenozoic tectonic uplift belt with SW-NE structural trend, constituting a pivotal tectonic unit between the Songliao Basin and Jiayi Fault Zone (Song et al., 2018). Tectonically characterized by relict volcanic arc fragments generated by the subduction of oceanic lithosphere associated with the Paleo-Asian Ocean (PAO), this belt preserves a complete magmatic sequence that systematically documents the geodynamic evolution of the eastern PAO, including successive stages of Late Paleozoic-Mesozoic oceanic crust subduction, continental margin collision, and orogenic development (Han et al., 2017; Li, 2023). Therefore, this region is a key part of the study of the evolution of the eastern section of the PAO and the focus of many scholars (Cao, 2013; Han et al., 2017; Song, 2018). Current academic consensus maintains that the Changchun-Yanji suture zone transecting the Daheishan Horst demarcates the final closure zone of PAO closure in its eastern segment (Cao, 2013; Song et al., 2018; Gao, 2024), with collisional termination temporally constrained to the late Permian-Middle Triassic interval (Wu et al., 2011; Zhou et al., 2011; Eizenhöfer et al., 2014; Liu J. et al., 2017; Ren et al., 2020; Jing et al., 2021; Zhang et al., 2024).

However, the tectonic setting of Late Permian magmatic rocks in the Daheishan Horst remains debated. Some researchers attribute their origin to Paleo-Asian Ocean subduction, based on: (1) Andean-type active continental margin rocks (diorite, hornblende gabbro, gabbroic diorite) north of the suture, and (2) Voluminous arc-affiliated intermediate-felsic suites with mantle wedge metasomatism signatures (high-Mg andesite, andesitic tuff and lava, rhyolite, gabbro-diorite) and subordinate mafic lithologies south of the suture (Guan et al., 2016; Wang, 2016; Han et al., 2017; Li, 2023; Jing, 2023). Consequently, two competing geodynamic models exist: Bidirectional subduction-collision along the Changchun-Yanji suture (Liu J. et al., 2017; Li, 2006; Song et al., 2018); Unidirectional subduction of the Paleo-Asian Ocean beneath the North China Craton (Cao et al., 2013; Yu et al., 2014; Wang Z. J. et al., 2015). Alternatively, Cao et al. (2013) relate this magmatism (e.g., bimodal volcanics, A-type granites) to post-collisional extension after the Middle Permian orogenic event. These persistent controversies, amplified by the horst's pivotal location, fundamentally impede reconstructing the tectonic evolution of the Paleo-Asian Ocean's eastern segment.

Integrating these tectonic debates, this study targets the altered diorite porphyry from Heibei Village, employing a multi-proxy analytical framework: (1) LA-ICP-MS zircon U-Pb geochronology, (2) Whole-rock major and trace element geochemistry (including rare earth elements), (3) Zircon Hf isotope analysis, and (4) Whole-rock Sr-Nd isotope analysis. Our results constrain the emplacement age and tectonic affinity of magmatic rocks in the Daheishan Horst, and further resolve the spatiotemporal patterns of subduction-to-closure processes along the Solonker-Xar Moron-Changchun-Yanji Suture (SXCYS) in the eastern Paleo-Asian Ocean. These findings establish critical constraints on the Paleo-Asian Ocean's evolution in central Jilin, while providing robust evidence for reconstructing Late Permian subduction-closure dynamics along its eastern segment.

2 Geological setting

The Daheishan Horst is tectonically located within the accretionary continental margin between the southeastern segment of the Xing-Meng Orogenic Belt and the North China Craton (Figure 1a). Bounded by the Siping-Dehui Fault (western boundary) and Yitong-Yilan Fault (eastern boundary, Qiu et al., 2024), this Meso- Cenozoic orogenic collage is flanked by the Songliao Basin to the west and adjoins the Yitong Graben to the east (Figure 1b). As a remnant of the eastern extension of the Xilamulun River Tectonic Belt, it is divided into northern and southern segments by the Xinlicheng Reservoir in Changchun (Li, 2012).

The study area is situated in the northeastern segment of the Daheishan Horst within central Jilin Province, where stratigraphic exposures exhibit structural discontinuity and have undergone intense metamorphism, with widespread coverage by Quaternary deposits. The regional stratigraphic succession includes the Permian sequences of the Paleozoic, such as the Madatun Formation (P_2m), which is dominated by tuffaceous and pyroclastic lithofacies, the Yangjiagou Formation (P_2y) characterized by dark-colored sandstone and siltstone assemblages, and the Yilaxi Formation (P_1y) consisting of andesite-tuffaceous conglomerate sequences; Mesozoic Triassic Lujiatun Formation (T_1l) featuring sandstone-siltstone intercalations, Cretaceous Quantou (K_1q) and Denglouku (K_1d) Formations containing conglomerate-sandstone-mudstone fluvial-lacustrine facies associations; and Cenozoic Paleogene (E) to Quaternary (Q) clastic sedimentary cover (Figure 1c).

The structural framework of the study area is dominated by NW-trending faults, with a secondary set of NS-trending fractures. Intense magmatic activities, influenced by polyphase tectonic-magmatic events, demonstrate NE-SW-trending zonal distribution patterns. The lithological assemblages display distinct zonation, mainly composed of plagiogranite, granodiorite, and intermediate to acidic volcanic rocks, including subordinate andesite and rhyolite, with granitoids predominantly occurring as batholithic masses. Dike swarms are well developed, primarily composed of diorite porphyry and granite porphyry, and locally exhibit intrusive relationships with the host plutons.

3 Sample description and analytical methods

The analyzed sample (HBC-YM) was collected from the northeastern part of Heibei Village, Jilin City, Jilin Province (126.18962235°E, 44.14666686°N). It is identified as an altered diorite porphyry with a brownish-gray color on the fresh surface and exhibits a massive texture (Figure 2a). The rock consists predominantly of groundmass and minor phenocrysts, and has undergone moderate to intense alteration, including sericitization, chloritization, and limonitization. Late-stage fractures (<0.3–0.01 mm in width) are developed and filled with calcite, quartz, and limonite. The sample displays a relict porphyritic texture, with the groundmass showing a fine-grained, subhedral granular texture. The groundmass makes up approximately 99% of the rock and consists mainly of subhedral plagioclase (Pl), amphibole, and iron-bearing minerals with minor quartz, with grain sizes ranging from <0.3 to 0.1 mm. Plagioclase exhibits slight sericitization,

10.3389/feart.2025.1639022

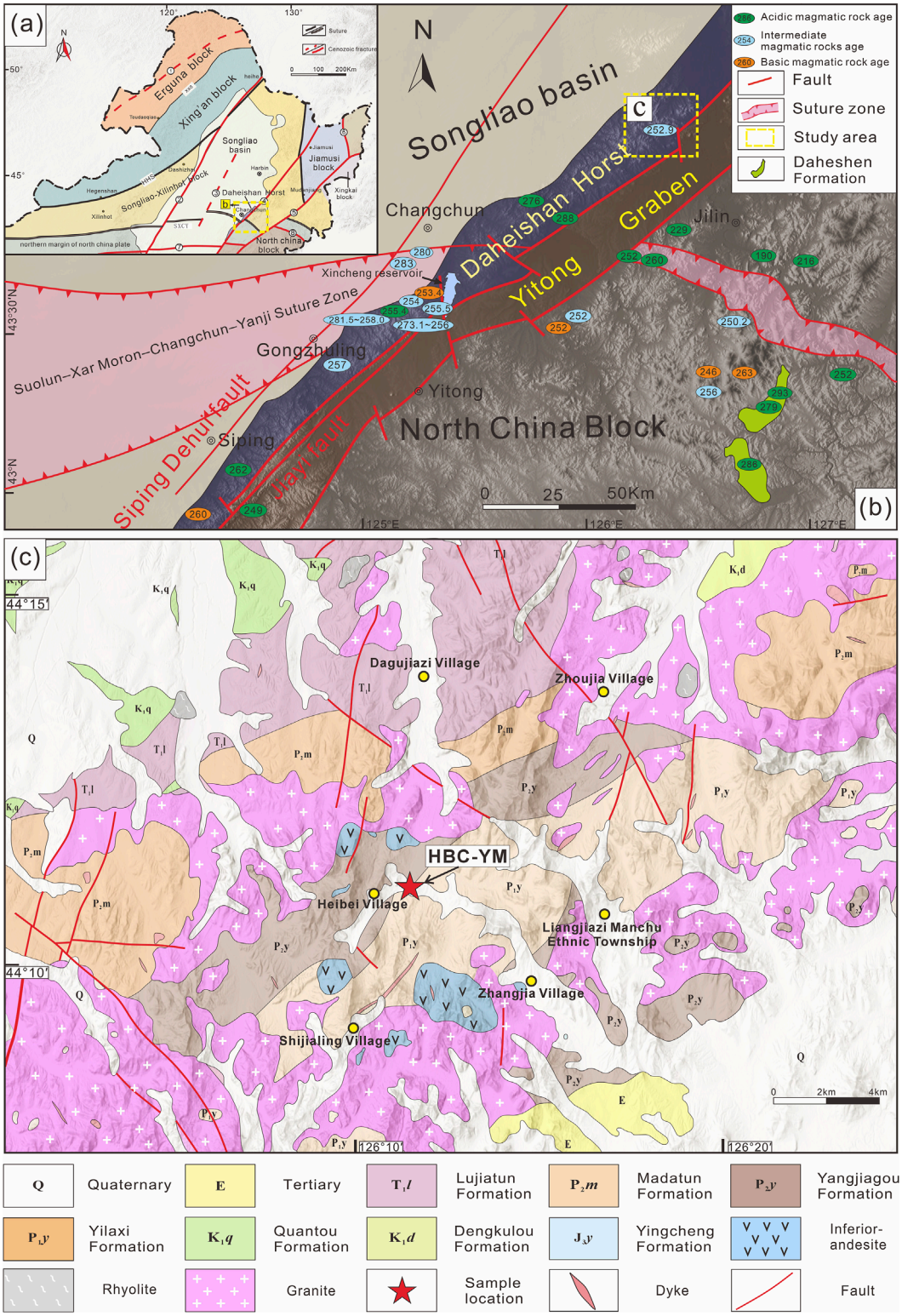

FIGURE 1
(a) Simplified geological map of Northeast China; **(b)** Simplified geotectonic units map of the Daheishan Horst; **(c)** simplified geological map of the study area. The abbreviations shown in the figure are: XXS, Xinlin-Xiguitu suture zone; HHS, Hegenshan-Heihe suture zone; SXCYS, Solonker-Xar Moron-Changchun-Yanji Suture Zone; F1, Derbugan Fault; F2, Nenjiang-Balihan Fault; F3, Central Songliao Basin Fault; F4, Jiamusi-Yilan Fault; F5, Dunhua-Mishan Fault; F6, Yuejinshan Fault; F7, Chifeng-Kaiyuan Fault; F8, Gudonghe-Fu'erhe Fault.

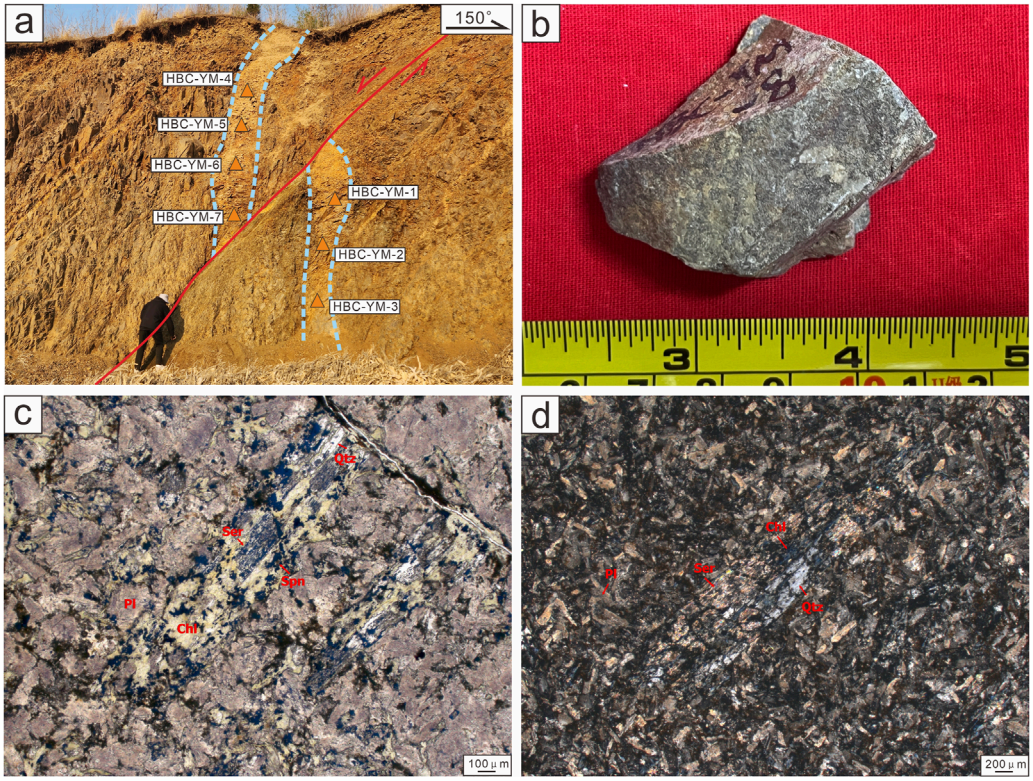

FIGURE 2
Field photographs and photomicrographs of brown-gray altered diorite porphyry. **(a)** Field photograph of brown-gray altered diorite porphyry; **(b)** Hand specimens of brown-gray altered diorite porphyry; **(c)** Photomicrograph of brown-gray altered diorite porphyry under plane-polarized light; **(d)** Photomicrograph of brown-gray altered diorite porphyry under cross-polarized light. The abbreviations shown in the figure are: Pl, plagioclase; Ser, sericite; Chl, chlorite; Qtz, quartz; Spn, sphene.

whereas amphibole has been completely altered to chlorite and sericite, accompanied by the exsolution of fine-grained titanite (Sphene) and ilmenite, retaining relict crystal outlines. Magnetite is fully oxidized to limonite. Estimated modal compositions are: plagioclase (~67%), amphibole (~32%), with trace amounts of quartz and iron oxides. Phenocrysts account for approximately 1% of the rock, consisting mainly of altered mafic minerals in subhedral prismatic forms (grain size <3.6–0.5 mm). These phenocrysts are completely replaced by sericite, chlorite, and quartz, and contain accessory titanite and ilmenite, preserving the original crystal morphology, indicating that the protolith was amphibole. These are unevenly distributed throughout the sample. Accessory minerals are minor, primarily apatite, occurring as acicular to prismatic crystals (<0.3–0.02 mm) with heterogeneous distribution (Figures 2b,c).

In this study, whole-rock geochemical analyses, including major, trace, and rare earth element (REE) concentrations, were performed at the Laboratory Center of Hebei Zhongtie Geophysical Prospecting Co., Ltd. Major elements were analyzed using an ARL Advant'XP+ X-ray fluorescence (XRF) spectrometer, with analytical precision generally better than 3%. Trace and rare earth elements were measured using an X-Series 2 ICP-MS (SN01831C), with analytical precision also better than 3%. Analytical procedures followed the methods described in Liu et al. (2016).

Zircon U–Pb isotopic dating was conducted *via* LA-ICP-MS at the Testing Center of China Metallurgical Geology Bureau, Shandong Bureau Group. Cathodoluminescence (CL) imaging of zircon grains was carried out using a JEOL JXA-8100 electron probe microanalyzer (EPMA) under an accelerating voltage of 15 kV and a beam current of 2×10^{-8} A. LA-ICP-MS zircon U–Pb analyses were conducted using a Thermo XSeries 2 mass spectrometer coupled with a COMPex Pro 193 nm ArF excimer laser ablation system (Coherent Inc.). Analytical parameters included a laser spot size of 30 μm, repetition rate of 8 Hz, and energy density of 8.5 J/cm^2. The total ablation duration was 110 s, consisting of 30 s for background signal acquisition, 55 s for ablation, and 25 s for signal washout. Detailed analytical protocols followed by Jackson et al. (2004). Data reduction was carried out using the ICPMSDataCal software (Liu et al., 2010b). Isotopic ratio calculations, age determinations, and common Pb corrections were based on the method of Andersen (2002). Concordia diagrams and age plots were generated using the ISOPLOT software.

Sr-Nd isotope analyses were conducted at the Isotope Laboratory, Institute of Geology, Chinese Academy of Geological Sciences. Separation of Sm and Nd followed a conventional two-stage ion exchange procedure: (1) Light rare earth elements (LREE) were separated on cation-exchange columns (1 × 8 cm; Bio-Rad AG50W-X8 resin, 200–400 mesh), and (2) Sm/Nd purification was achieved using columns (0.6 × 7 cm) packed with Kel-F powder coated with HDEHP (diethylhexyl phosphoric acid) as the stationary phase. Isotopic measurements were performed

on a Finnigan MAT-261 mass spectrometer equipped with 7 Faraday collectors, operating in static multi-collection mode for Sr and dynamic mode for Nd. The measured $^{87}Sr/^{86}Sr$ ratios were normalized to $^{86}Sr/^{88}Sr = 0.1194$, with NBS-607 standard yielding $^{87}Sr/^{86}Sr = 1.20035 \pm 0.00001$ ($2\sigma_m$, n = 6). $^{143}Nd/^{144}Nd$ ratios were normalized to $^{146}Nd/^{144}Nd = 0.7219$, and the La Jolla standard gave $^{143}Nd/^{144}Nd = 0.511854 \pm 0.000007$ ($2\sigma_m$, n = 8). Decay constants used for age calculations were $\lambda^{87}Rb = 0.0142\ Ga^{-1}$ and $\lambda^{147}Sm = 0.00654\ Ga^{-1}$.

Experiments were conducted using a Neptune Plus MC-ICP-MS (Thermo Fisher Scientific) in combination with a Geolas Pro excimer ArF laser ablation system (Coherent). Helium was used as the carrier gas within the ablation cell (Hu Z. C. et al., 2008) merged with argon (makeup gas) and small amounts of nitrogen (8 mL min^{-1}) after the ablation cell, and the newly designed X skimmer cone and Jet sample cone in Neptune Plus were used in the experiments in order to improved the signal intensity (Hu Z. et al., 2008). In addition, a "wire" signal smoothing device is included in this laser ablation system, by which smooth signals are produced even at very low laser repetition rates down to 1 Hz (Hu Z. et al., 2012). The energy density of laser ablation that was used in this study was 3–5 J cm^{-2}, and all data were acquired on zircon in single spot ablation mode at a spot size of 44 μm. Detailed instrument operating conditions and analysis methods can be referred to Hu Z. C. et al. (2012). We applied the directly obtained β_{Yb} value from the zircon sample itself in real-time in this study. The $^{179}Hf/^{177}Hf$ and $^{173}Yb/^{171}Yb$ ratios were used to calculate the mass bias of Hf (β_{Hf}) and Yb (β_{Yb}), which were normalised to $^{179}Hf/^{177}Hf = 0.7325$ and $^{173}Yb/^{171}Yb = 1.132685$ (Fisher et al., 2014) using an exponential correction for mass bias. Interference of ^{176}Yb on ^{176}Hf was corrected by measuring the interference-free ^{173}Yb isotope and using $^{176}Yb/^{173}Yb = 0.79639$ (Fisher et al., 2014) to calculate $^{176}Yb/^{177}Hf$. Similarly, the relatively minor interference of ^{176}Lu on ^{176}Hf was corrected by measuring the intensity of the interference-free ^{175}Lu isotope and using the recommended $^{176}Lu/^{175}Lu = 0.02656$ (Blichert-Toft et al., 1997) to calculate $^{176}Lu/^{177}Hf$. We used the mass bias of Yb (β_{Yb}) to calculate the mass fractionation of Lu because of their similar physicochemical properties. Off-line selection and integration of analyte signals, and mass bias calibrations were performed using ICPMSDataCal (Liu et al., 2010a).

4 Analytical results

4.1 Zircon U–Pb geochronology

The U-Pb zircon isotopic dating results for sample HBC-YM-7 are summarized in Table 1. Cathodoluminescence (CL) imaging of analyzed zircons (Figure 3c) reveals predominantly euhedral to subhedral crystals with well-preserved morphological features, distinct crystal edges, and clear internal structures displaying magmatic oscillatory zoning. The analyzed zircons exhibit U concentrations ranging from 90×10^{-6} to 1052×10^{-6} (average 379×10^{-6}) and Th concentrations from 59×10^{-6} to 392×10^{-6} (average 206×10^{-6}), yielding Th/U ratios of 0.28–0.82 (mean 0.59), consistent with magmatic zircon characteristics.

A total of 30 zircon spots were conducted, with 11 spots yielding $^{206}Pb/^{238}U$ ages ranging from 240 to 256 Ma. The weighted mean $^{206}Pb/^{238}U$ age of 252.9 ± 3.2 Ma (MSWD = 1.5; n = 11) defines the emplacement timing of the diorite porphyry in the Daheishan Horst during the Late Permian (Figures 3a,b). Eight analytical spots (HBC-YM-7-02, 04, 06, 08, 09, 25, 27, 28) were excluded due to short signal durations (<20 s, standard acquisition ~40 s), likely caused by thin zircon domains or laser ablation breakthrough, which could result in spuriously young age values. Five zircon grains yielded older $^{206}Pb/^{238}U$ ages of 490, 1,118, 1,598, 2,158, and 2,462 Ma, interpreted as inherited components incorporated during magma ascent. An additional six grains produced anomalously young $^{206}Pb/^{238}U$ ages, likely attributable to partial recrystallization, metamorphic overprinting, or contamination from younger lithologies (e.g., Cenozoic sediments) during sample preparation.

4.2 Geochemical signatures of major oxides

The diorite porphyry sample (HBC-YM) from the Daheishan Horst displays characteristic major element geochemistry (Table 2), with SiO_2 contents ranging 54.17–55.65 wt%, TiO_2 1.31–1.34 wt%, Al_2O_3 16.98–18.71 wt%, MgO 2.52–3.3 wt%, and CaO 3.18–3.94 wt%. Its alkali geochemistry reveals sodic affinity ($Na_2O + K_2O$ = 7.26–7.77 wt%; Na_2O/K_2O ratio = 2.44–5.63), showing Na-enrichment and K-depletion features. Petrological classification based on standardized diagrams shows that: (1) the TAS (Total Alkali-Silica) diagram (Figure 4a) plots the sample in the basaltic trachyandesite field; (2) the K_2O vs SiO_2 diagram (Figure 4b) indicates a medium-K calc-alkaline affinity, consistent with magma generation in an active continental margin setting.

4.3 Trace and rare earth elements (REE)

The trace and rare earth element (REE) concentrations of the diorite porphyry samples from the Daheishan Horst are summarized in Table 2. Whole-rock geochemistry reveals total REE contents ranging from 172.06 to 196.52 ppm, with light REE (LREE: La-Sm) concentrations varying between 132.91 and 152.85 ppm, and heavy REE (HREE: Eu-Lu) contents from 16.89 to 19.04 ppm. These rocks display significant LREE enrichment relative to HREE (LREE/HREE = 7.86–9.05), indicating pronounced fractionation between light and heavy rare earth elements. The chondrite-normalized REE patterns (Figure 5a) demonstrate characteristic right-inclined profiles with steep LREE-enriched slopes and relatively flat HREE segments, indicative of strong LREE/HREE fractionation. Primitive mantle-normalized trace element diagrams (Figure 5b) reveal distinct geochemical signatures: marked enrichment in large-ion lithophile elements (LILEs; e.g., Rb, Th, U, K), along with notable depletion in high-field-strength elements (HFSEs; e.g., Nb, Ta, P, Ti). This geochemical fingerprint, showing remarkable similarity to upper continental crust compositional trends, exhibits diagnostic features comparable to magmatic suites from arc-related environments or active continental margin tectonic settings.

TABLE 1 LA-ICP-MS zircon U-Pb dating results of the quartz diorite porphyry in the "Daheishan Horst".

Sample	Th (10^{-6})	U (10^{-6})	Th/U	$^{207}Pb/^{206}Pb$	1σ	$^{207}Pb/^{235}U$	1σ	$^{206}Pb/^{238}U$	1σ	$^{208}Pb/^{232}Th$	1σ	年龄(Ma)					
												$^{207}Pb/^{235}U$	1σ	$^{206}Pb/^{238}U$	1σ	$^{208}Pb/^{232}Th$	1σ
HBC-YM-7-001	59	90	0.65	0.0563	0.0061	0.2847	0.0281	0.0380	0.0011	0.0116	0.0008	254	22	240	7	233	17
HBC-YM-7-003	425	425	1.00	0.0549	0.0021	0.2321	0.0092	0.0308	0.0005	0.0096	0.0003	212	8	195	3	192	6
HBC-YM-7-005	239	292	0.82	0.0506	0.0017	0.2790	0.0093	0.0401	0.0006	0.0123	0.0003	250	7	254	4	246	7
HBC-YM-7-007	105	181	0.58	0.0536	0.0026	0.2253	0.0107	0.0307	0.0005	0.0101	0.0004	206	9	195	3	203	8
HBC-YM-7-010	164	601	0.27	0.0583	0.0012	0.6374	0.0140	0.0790	0.0009	0.0244	0.0006	501	9	490	6	487	12
HBC-YM-7-011	255	297	0.86	0.0503	0.0044	0.0655	0.0044	0.0099	0.0003	0.0034	0.0002	64	4	63	2	69	4
HBC-YM-7-012	269	446	0.60	0.0554	0.0015	0.3059	0.0077	0.0405	0.0007	0.0133	0.0003	271	6	256	4	267	6
HBC-YM-7-013	344	270	1.28	0.0547	0.0020	0.2488	0.0094	0.0330	0.0005	0.0102	0.0002	226	8	209	3	205	5
HBC-YM-7-014	231	381	0.61	0.0520	0.0015	0.2771	0.0080	0.0387	0.0005	0.0121	0.0003	248	6	245	3	244	6
HBC-YM-7-015	241	219	1.10	0.0508	0.0029	0.1182	0.0063	0.0172	0.0003	0.0054	0.0002	113	6	110	2	109	3
HBC-YM-7-016	78	177	0.44	0.0547	0.0040	0.2982	0.0136	0.0401	0.0007	0.0185	0.0010	265	11	253	4	371	20
HBC-YM-7-017	392	483	0.81	0.0502	0.0016	0.2777	0.0081	0.0403	0.0007	0.0123	0.0003	249	6	255	4	247	6
HBC-YM-7-018	155	256	0.60	0.0540	0.0020	0.3013	0.0114	0.0404	0.0006	0.0128	0.0004	267	9	255	4	256	8
HBC-YM-7-019	107	169	0.63	0.0505	0.0026	0.2781	0.0129	0.0404	0.0009	0.0125	0.0005	249	10	255	5	252	9

(Continued on the following page)

10.3389/feart.2025.1639022

TABLE 1 (*Continued*) LA-ICP-MS zircon U-Pb dating results of the quartz diorite porphyry in the "Daheishan Horst".

Sample	Th (10^{-6})	U (10^{-6})	Th/U	$^{207}Pb/^{206}Pb$	1σ	$^{207}Pb/^{235}U$	1σ	$^{206}Pb/^{238}U$	1σ	$^{208}Pb/^{232}Th$	1σ	年龄(Ma)					
												$^{207}Pb/^{235}U$	1σ	$^{206}Pb/^{238}U$	1σ	$^{208}Pb/^{232}Th$	1σ
HBC-YM-7-020	268	467	0.57	0.1606	0.0025	9.0737	0.1596	0.4066	0.0048	0.1155	0.0023	2,345	16	2,200	22	2,209	41
HBC-YM-7-021	295	1053	0.28	0.0510	0.0026	0.2865	0.0071	0.0405	0.0006	0.0149	0.0004	256	6	256	3	299	9
HBC-YM-7-022	261	450	0.58	0.0520	0.0017	0.2901	0.0089	0.0404	0.0006	0.0122	0.0003	259	7	256	3	244	6
HBC-YM-7-023	179	375	0.48	0.0522	0.0016	0.2904	0.0085	0.0404	0.0006	0.0128	0.0004	259	7	256	4	256	7
HBC-YM-7-024	169	180	0.94	0.0526	0.0028	0.2313	0.0106	0.0324	0.0005	0.0104	0.0003	211	9	206	3	210	6
HBC-YM-7-026	43	90	0.48	0.1345	0.0023	7.6489	0.1500	0.4098	0.0054	0.1186	0.0031	2,191	18	2,214	25	2,264	56
HBC-YM-7-028	215	365	0.59	0.0593	0.0040	0.0616	0.0037	0.0078	0.0002	0.0027	0.0001	61	4	50	1	55	3
HBC-YM-7-029	28	61	0.46	0.1134	0.0028	4.4039	0.1146	0.2813	0.0043	0.0904	0.0026	1713	22	1598	22	1749	48
HBC-YM-7-030	385	331	1.16	0.0774	0.0022	2.0295	0.0428	0.1894	0.0025	0.0596	0.0014	1125	14	1118	14	1170	27

10.3389/feart.2025.1639022

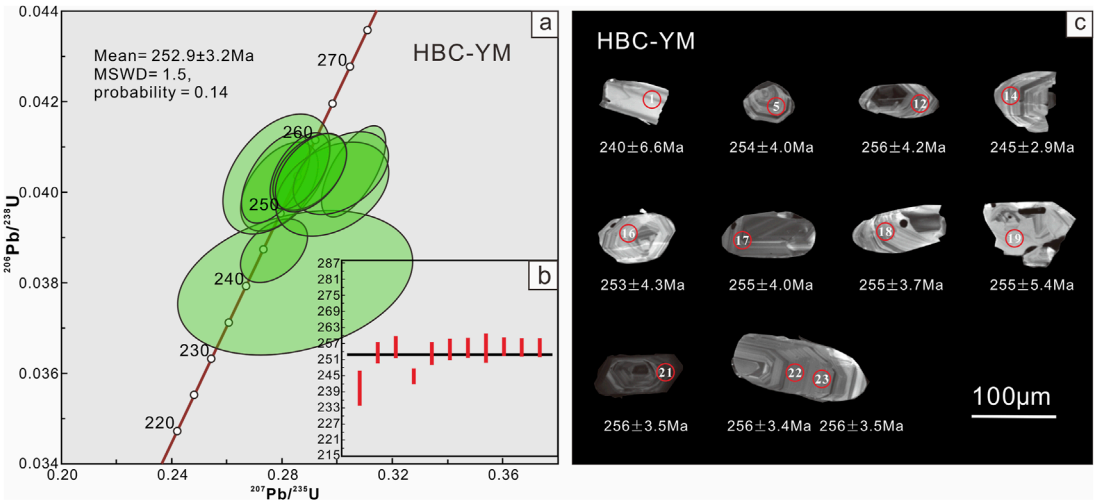

FIGURE 3
Zircon LA-ICP-MS U-Pb age diagrams of diorite porphyry samples: **(a)** Concordia diagram; **(b)** Weighted mean age plot; **(c)** Cathodoluminescence (CL) images of representative zircon grains.

4.4 *In-situ* zircon Hf isotopic characteristics

Seventeen *in-situ* zircon Hf isotope analyses were performed on sample HBC-YM-7 (diorite porphyry) from the Daheishan Horst. Three analytical spots were discarded due to laser-induced fracturing during ablation, leaving 14 valid analyses representing zircon crystallization at ~252.9 Ma. These yield $^{176}Hf/^{177}Hf$ ratios of 0.282650–0.282933, $\varepsilon Hf(t)$ values of +1.08 to +11.03, single-stage Hf model ages (T_{DM1}) of 457–856 Ma, and two-stage model ages (T_{DM2}) of 534–1090 Ma.

All $\varepsilon Hf(t)$ values are positive (>0), with data points plotting between the depleted mantle evolution curve and the chondritic uniform reservoir (CHUR) reference line (Figures 6a,b). This signature distinctly differs from the negative Hf isotopes characteristic of the Yanshan Orogen but aligns with Phanerozoic rocks in the eastern Xing'an-Mongolia Orogenic Belt (Yang et al., 2007). Complete analytical data are provided in Table 3.

4.5 Whole-rock Sr–Nd isotopic characteristics

Whole-rock Sr–Nd isotopic analyses of HBC-YM samples are presented in Table 4 and Figure 6c. The samples exhibit significant Rb–Sr compositional variations. Sample HBC-YM-1 (Rb = 118 ppm, Sr = 83.3 ppm, Rb/Sr = 1.42) shows an anomalously low initial $^{87}Sr/^{86}Sr$ ratio (0.690555), suggesting possible analytical disturbance given its high Rb/Sr ratio. In contrast, samples HBC-YM-2 and HBC-YM-3 display lower Rb/Sr ratios (0.025–0.077) and geochemically plausible initial $(^{87}Sr/^{86}Sr)_i$ values (0.704601–0.705469), consistent with mantle-derived signatures. These samples yield positive $\varepsilon Nd(t)$ values (+5.15 to +5.24) with two-stage Nd model ages (T_{DM2}) of 606–598 Ma.

5 Discussion

5.1 Geochronology of magmatic rocks in the Daheishan horst

Previous studies have extensively investigated the geochronology of magmatic rocks within the Daheishan Horst. Early researchers, based on regional stratigraphic correlation, proposed that the magmatic emplacement was contemporaneous with the metamorphic volcanic rocks of the Taoshan Formation (420.3 ± 6.47 Ma; Jiang, 2014), suggesting an Early-Middle Silurian formation age (Peng et al., 1979; Jia, 1990; Wu, 1994; Zhao, 1996; Wang and Su, 1996). Additionally, Gao (1985) inferred a Late Paleozoic origin through integrated stratigraphic analysis and whole-rock Rb-Sr dating methodology. Recent advances in zircon U-Pb geochronology (Figure 1b) have demonstrated that these magmatic rocks were emplaced during the Early to Late Permian (293–252.9 Ma; Han et al., 2017; Cao, 2013; Song, 2018), thereby challenging the conventional perspective of Early Paleozoic formation. The crystallization age of ~252.9 Ma obtained from our HBC-YM sample further corroborates previous findings, confirming its genetic affiliation with Late Paleozoic magmatic activity.

Previous studies have demonstrated that subduction-related magmatic rocks along the southern segment of the Permian Daheishan Horst were emplaced during 283–253 Ma (Han et al., 2017; Song, 2018; Mou, 2022). This temporal framework contrasts with the northern segment where subduction-generated magmatism occurred earlier (293–276 Ma; Shi et al., 2020), indicating distinct temporal patterns of magmatism between the two segments and a potentially longer duration of subduction in

TABLE 2 Whole rock REE and trace element data of magmatic rock samples from the Daheishan Horst.

Sample	HBC-YM-1	HBC-YM-2	HBC-YM-3	HBC-YM-4	HBC-YM-5	HBC-YM-6
SiO_2	54.94	55.30	54.08	54.82	55.57	55.30
Al_2O_3	17.56	17.81	18.00	18.69	18.27	16.96
TFe_2O_3	6.65	6.28	6.17	6.09	6.22	6.30
MgO	3.30	2.52	3.04	2.87	2.87	3.03
CaO	3.30	3.62	3.93	3.31	3.17	3.72
Na_2O	6.62	5.20	5.95	5.97	5.42	6.59
K_2O	1.11	2.13	1.54	1.78	1.84	1.17
MnO	0.082	0.109	0.080	0.079	0.076	0.086
P_2O_5	0.355	0.369	0.359	0.353	0.347	0.354
TiO_2	1.34	1.32	1.32	1.33	1.31	1.31
LOI	4.61	5.20	5.36	4.57	4.77	5.01
Li	32.2	40.6	40.2	40.3	37.8	37.8
Be	2.45	1.53	1.97	1.70	1.76	1.71
Sc	11.7	20.1	21.3	22.1	18.6	16.7
V	54.6	120	126	122	124	121
Co	7.74	16.3	25.3	17.7	18.0	20.2
Ni	14.4	12.8	16.3	13.1	13.2	13.8
Cu	14.1	34.5	42.4	28.5	40.8	41.3
Zn	68.5	84.7	88.6	82.7	81.7	83.4
Ga	18.4	20.6	22.1	22.5	21.4	21.1
Rb	118	26.8	62.9	39.9	45.7	55.4
Sr	83.3	1067	815	1124	929	856
Zr	257	231	251	249	237	246
Nb	13.3	4.44	4.60	4.52	4.42	4.61
Mo	0.62	0.47	0.51	0.42	0.36	0.35
In	0.065	0.048	0.052	0.056	0.049	0.049
Cs	5.76	2.39	5.29	3.98	3.67	3.73
Ba	541	300	534	402	469	479
Hf	7.43	6.01	6.43	6.43	6.11	6.24
Ta	0.89	0.33	0.45	0.37	0.29	0.29

(Continued on the following page)

TABLE 2 (*Continued*) Whole rock REE and trace element data of magmatic rock samples from the Daheishan Horst.

Sample	HBC-YM-1	HBC-YM-2	HBC-YM-3	HBC-YM-4	HBC-YM-5	HBC-YM-6
W	1.47	0.43	0.34	0.48	0.44	0.44
Tl	0.72	0.16	0.39	0.23	0.27	0.32
Pb	18.4	6.81	13.8	8.18	6.82	23.1
Bi	0.17	0.055	0.14	0.045	0.070	0.14
Th	11.7	6.21	6.65	6.54	6.23	6.55
U	2.80	1.52	1.70	1.52	1.53	1.65
Cr	33.0	14.1	8.92	8.06	9.28	7.76

Note: Major elements are reported in wt.% (weight percent); trace elements are reported in 10^{-6} (parts per million, ppm); LOI (Loss on Ignition) is given in wt.%.

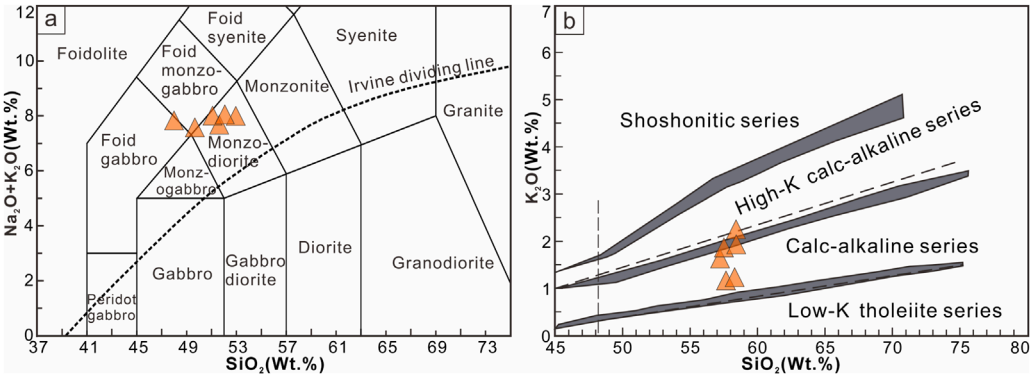

FIGURE 4
Petrological classification diagrams of Daheishan magmatic rocks. **(a)** Total alkalis ($Na_2O + K_2O$) *versus* SiO_2 classification diagram (after Middlemost, 1994); **(b)** K_2O vs SiO_2 (after Rickwood, 1989).

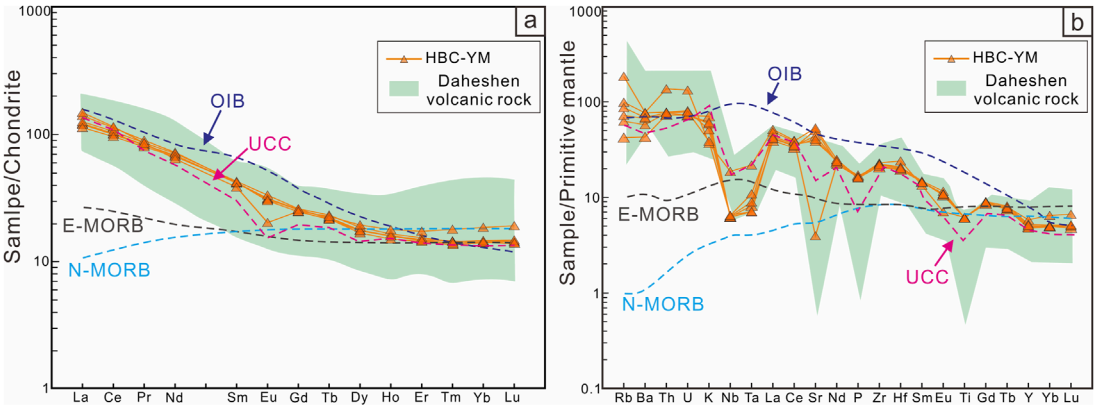

FIGURE 5
(a) Chondrite-normalized REE patterns and **(b)** primitive-mantle-normalized trace element spidergram. Chondrite-normalised and primitive-mantle-normalized values are after Sun and McDonough (1989). Daheshen volcanic rock data from Cao et al. (2012). The abbreviations shown in the figure are: OIB, Ocean Island Basalt; N-MORB, Normal Mid-Ocean Ridge Basalt; E-MORB, Enriched Mid-Ocean Ridge Basalt; UCC, Upper Continental Crust.

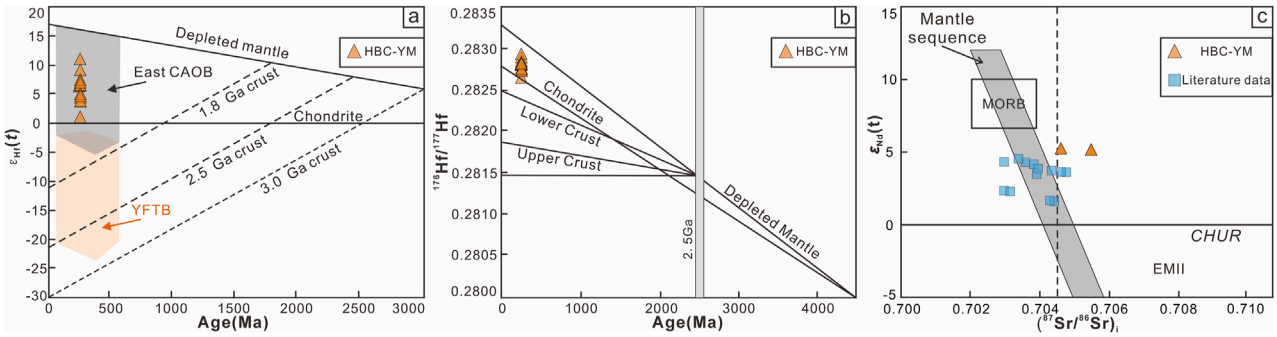

FIGURE 6
. Zircon andepsi;Hf(t) vs age diagrams [**(a, b)**, modified after Yang et al. (2007)], and whole-rock andepsi;Nd(t) vs $(^{87}Sr/^{86}Sr)_i$ diagram [**(c)**, modified after Yu et al. (2014); data cited from Song (2018)]. The abbreviations shown in the figure are: YFTB, Yanshan Fold-and-Thrust Belt; CAOB, Central Asian Orogenic Belt; MORB, Mid-Ocean Ridge Basalt; EMII, Enriched Mantle Type II; CHUR, Chondritic Uniform Reservoir.

TABLE 3 Lu–Hf isotopic analytical results of zircons from the dioritic porphyrite sample.

Sample	*t* (Ma)	$^{176}Yb/^{177}Hf$	$^{176}Lu/^{177}Hf$	$^{176}Hf/^{177}Hf$	1σ	εHf(t)	1σ	T_{DM1}	T_{DM2}	$f_{Lu/Hf}$
HBC-YM-7										
HBC-YM-7-02	254	0.031974	0.001178	0.282650	0.699916	1.08	0.72	856	1090	−0.96
HBC-YM-7-04	245	0.035580	0.001452	0.282806	0.724683	6.36	0.74	639	789	−0.96
HBC-YM-7-05	255	0.119165	0.004508	0.282894	0.856792	9.17	0.87	559	640	−0.86
HBC-YM-7-06	255	0.120205	0.004550	0.282851	1.098542	7.64	1.11	627	725	−0.86
HBC-YM-7-07	255	0.031578	0.001269	0.282804	0.915345	6.51	0.93	640	788	−0.96
HBC-YM-7-08	255	0.042540	0.001700	0.282808	0.676496	6.58	0.70	642	785	−0.95
HBC-YM-7-09	256	0.043606	0.001630	0.282744	0.750052	4.36	0.77	732	909	−0.95
HBC-YM-7-10	256	0.054337	0.002019	0.282730	0.730448	3.78	0.75	761	941	−0.94
HBC-YM-7-11	256	0.052602	0.002047	0.282730	0.726786	3.79	0.74	761	940	−0.94
HBC-YM-7-12	256	0.029061	0.001139	0.282761	0.695486	5.06	0.71	698	870	−0.97
HBC-YM-7-13	256	0.021875	0.000889	0.282750	0.675020	4.68	0.69	710	891	−0.97
HBC-YM-7-14	253	0.037364	0.001502	0.282934	0.741165	11.03	0.76	457	534	−0.95
HBC-YM-7-16	255	0.025151	0.001042	0.282830	0.732957	7.49	0.75	599	734	−0.97
HBC-YM-7-17	255	0.025701	0.001051	0.282817	0.651805	7.02	0.67	617	760	−0.97

the southern domain (Figure 1b). This study reports, for the first time, the identification of subduction-affinity magmatic rocks dated at ~252.9 Ma in the northern Daheishan Horst. This discovery extends the magmatic activity window of the northern segment to 288–252.9 Ma, revealing substantial temporal overlap with the southern segment's magmatic record (283–253 Ma). The coeval magmatic manifestations across both segments imply that the Daheishan Horst likely experienced a unified tectono-magmatic event during the Permian period.

5.2 Petrogenesis and tectonic setting of magmatic rocks in the Daheishan horst

Both the diorite porphyry samples analyzed in this study and the Daheshen Formation magmatic suite in the Huadian area (Figure 1b; Cao et al., 2012) exhibit a calc-alkaline affinity. Whole-rock geochemical analyses reveal that these samples share remarkable geochemical congruity: (1) Chondrite-normalized rare earth element (REE) patterns exhibit consistent enrichment in

10.3389/feart.2025.1639022

TABLE 4 Whole-rock Sr–Nd isotopic compositions of the dioritic porphyrite sample.

Sample	t (Ma)	Rb (ppm)	Sr (ppm)	$^{87}Rb/^{86}Sr$	$^{87}Sr/^{86}Sr$	±2SE	Sm (ppm)	Nd (ppm)	$^{147}Sm/^{144}Nd$	$^{143}Nd/^{144}Nd$	±2SE	$(^{87}Sr/^{86}Sr)_i$	ε_{Nd} (0)	ε_{Nd}(t)	$T_{DM1(Ma)}$	$T_{2DM(Ma)}$	$f_{Sm/Nd}$
HBC-YM-1	252.9	118	83.3	4.0945	0.705268	0.0000184	5.94	30.1	0.1194	0.512774	0.0000079	0.690555471	2.65	5.15	611	606	−0.39
HBC-YM-2	252.9	26.8	1067	0.0726	0.70573	0.0000159	6.45	31.4	0.1242	0.512783	0.0000076	0.705469133	2.83	5.16	628	604	−0.37
HBC-YM-3	252.9	62.9	815	0.2236	0.705405	0.0000158	6.58	33.3	0.1196	0.512779	0.0000083	0.704601465	2.75	5.24	604	598	−0.39

light rare earth elements (LREEs) coupled with depletion in heavy rare earth elements (HREEs), manifesting characteristic right-inclined REE distribution patterns (Figure 5a); (2) Primitive mantle-normalized trace element spider diagrams (Figure 5b) display significant enrichment in large-ion lithophile elements (LILEs; e.g., Rb, Th, U, K) alongside pronounced depletion in high-field-strength elements (HFSEs; Nb, Ta, P, Ti), displaying distinct geochemical signatures that are markedly different from those of OIB, E-MORB, and N-MORB basalts. Notably, previous petrogenetic studies have established that the Daheshen Formation magmatic rocks possess diagnostic geochemical fingerprints of active continental margin settings, interpreted as products of PAO plate subduction (Cao et al., 2012). This geochemical coherence, particularly the characteristic LILE/HFSE fractionation patterns and calc-alkaline affinity, strongly suggests that the Daheishan Horst diorite porphyry likely originated through similar subduction-related processes within an active continental margin framework. These two magmatic suites are both interpreted as Permian arc-related products developed along the Solonker–Xar Moron–Changchun–Yanji suture zone, offering important petrogenetic constraints for understanding the closure of the Paleo-Asian Ocean.

In-situ zircon Hf isotopic analyses for the diorite porphyry samples yield εHf(t) values of +1.08 to +11.03, with a mean value of +6.04 and median of +6.4. Corresponding two-stage Hf model ages (T_{DM2}) range from 534 to 1090 Ma. These values exhibit strong consistency with the Hf isotopic spectrum of Phanerozoic igneous rocks in the Central Asian Orogenic Belt (CAOB) (Figures 6a,b; Yang et al., 2007; Cao, 2013), indicating derivation of the magmatic source primarily from: a subduction-fluid-metasomatized depleted mantle or Neoproterozoic–Early Paleozoic juvenile crust accreted during CAOB evolution. Although subordinate analyses show lower εHf(t) values (down to +1.08), potentially reflecting minor assimilation of ancient crustal materials or inherited zircon effects, these contributions do not overprint the dominant juvenile isotopic signature.

Combined with whole-rock Sr–Nd isotopic signatures ($(^{87}Sr/^{86}Sr)_i$ = 0.704601–0.705469, εNd(t) = +5.15 to +5.24, (T_{DM2}) = 606–598 Ma), the data points cluster proximal to the mantle array. This further corroborates that the magmas were dominantly generated by partial melting of a depleted mantle source, with negligible contamination from ancient continental crust.

Critically, post-magmatic hydrothermal alteration has affected the studied diorite porphyry samples, potentially compromising the accuracy of their initial $^{87}Sr/^{86}Sr$ ratios. To validate the robustness of the observed signatures, we compiled Sr-Nd data from pristinely preserved Late Permian igneous rocks along the southern suture zone of the Daheishan Horst (Song, 2018). Collectively, these datasets demonstrate coherent depleted mantle-like Sr-Nd isotopic compositions (Figure 6c), confirming a regionally depleted mantle source beneath the Daheishan Horst.

Previous studies have demonstrated that the relationship between La/Sm ratios and La concentrations is a key geochemical indicator for evaluating rare earth element (REE) fractionation behavior. This method is widely used to distinguish magmatic processes controlled by fractional crystallization from those dominated by partial melting (Allègre and Minster, 1978; Zhang, 2024). Diagnostic patterns emerge in La/Sm-La systematics: (1) Horizontally aligned data points (constant La/Sm ratios with

variable La concentrations) typically indicate melt differentiation through fractional crystallization from a common parental magma; (2) Positive correlations between La/Sm and La abundances suggest melt generation *via* progressive partial melting of a compositionally homogeneous source. In the La/Sm-La discrimination diagram (Figure 7b), the studied samples exhibit a co-varying increase in La/Sm ratios and La concentrations. This geochemical trajectory demonstrates enhanced light rare earth element (LREE) fractionation and precludes fractional crystallization as the dominant process. The observed compositional variability in diorite porphyry samples is therefore attributed to either variable degrees of partial melting or inherent geochemical heterogeneity within the source region.

This is a key geochemical indicator of continental crustal materials and subducted sediments, and is widely used to constrain the petrogenesis and tectonic settings of basaltic systems. In active continental margin settings, typical samples plot in the high-Th (>5 ppm) and intermediate-to-low Ta-Hf/3 (0–2) field (Wood et al., 1979). In the Th-Ta-Hf/3 discrimination diagram (Figure 7a), the studied diorite porphyries from the Daheishan Horst exhibit elevated Th contents (6.21–11.66 ppm) with moderate Ta-Hf/3 ratios, geochemically consistent with intermediate-acid volcanic rocks in the southern segment of this belt (Han et al., 2017; Song, 2018). All samples fall within the calc-alkaline basalt series field, which is characteristic of subduction-related arc environments, indicating typical magmatic affinities of ocean-continent subduction zones.

Additionally, the Nb/Yb ratio is routinely employed to reflect the enrichment-depletion relationships in mantle source regions. The selection of Yb as the denominator minimizes the effects of partial melting and fractional crystallization, enabling reliable retrieval of source mantle compositions through petrogenetic inversions. Geochemical thresholds indicate: Nb/Yb = 0.5–1.5 characterizes transitional regimes between subduction-related depletion (low Nb/Yb) and intraplate enrichment (high Nb/Yb), whereas Nb/Yb < 0.5 reflects extreme depletion in oceanic arc settings. Th/Yb ratios greater than one are considered quantitative indicators of crustal assimilation or subducted sediment input into magmatic sources (Pearce and Peate, 1995). In the Yb-normalized Th-Nb covariation diagram (Figure 7c), samples investigated in this study exhibit Th/Yb ratios of 2.52–3.66 and Nb/Yb values >0.5. These geochemical signatures align with intermediate-acid volcanic rocks from the southern Daheishan Horst (Han et al., 2017; Song, 2018), collectively plotting within the overlapping field between continental arc basalts (CAB) and oceanic arc basalts (OAB), and a pronounced clustering trend toward the continental arc basalt (CAB) domain. It is noteworthy that although both oceanic island arc and active continental margin basalts are genetically associated with subduction-related processes, they exhibit distinct geochemical signatures. Typical oceanic island arc basalts are characterized by low Zr/Y ratios (<3.3) and Ta/Yb ratios (<0.1). In contrast, basalts from active continental margins display relatively elevated La/Zr and Nb/Zr ratios, with a discriminant boundary defined by $La \times Nb/Zr^2 = 0.002$ (Wood D.A., 1980; Pearce, 1982; Sun et al., 2007; Han et al., 2017). The magmatic rocks from the Daheishan Horst exhibit Zr/Y ratios ranging from 9.7 to 11.5 (>3), Ta/Yb ratios from 0.12 to 0.28 (>0.1), and $La \times Nb/Zr^2$ values between 0.002 and 0.007 (>0.002), indicating a pronounced continental affinity. These geochemical characteristics rule out the possibility that the samples are oceanic island arc basalts, suggesting instead that they may represent basalts formed in an active continental margin setting or intraplate basalts contaminated by crustal materials. Additionally, the Nb/Zr ratios of the dioritic porphyrite samples analyzed in this study range from 0.018 to 0.052, with one anomalously high value (0.052) and the remaining five samples all falling below 0.02. These values are significantly lower than those typical of intraplate basalts (Nb/Zr >0.04; Wood, 1980), thereby excluding an intraplate basalt origin.

Collectively, the Late Permian diorite porphyry samples from the Daheishan Horst originated from partial melting of a subduction-fluid-metasomatized mantle source, constrained by depleted Hf-Nd isotopes, and were generated through subduction processes beneath an active continental margin.

5.3 Evolutionary processes of the eastern segment of the PAO

The tectonic evolution of the eastern PAO during its subduction remains controversial, with two competing models proposed for the SXCYS: 1) a bidirectional subduction-collision closure model (Liu J. et al., 2017; Song, 2018; Jing, 2023) *versus* 2) a unidirectional subduction model (Cao et al., 2013; Yu et al., 2014; Wang Z. J. et al., 2015). Recent paleomagnetic data suggests that the Late Carboniferous-Early Permian eastern PAO segment along the southern Xing-Meng Orogenic Belt exhibited a trumpet-shaped configuration with eastward-propagating expansion (Zhang et al., 2021). Provenance analysis from the northern margin of the North China Craton further indicates a diachronous closure of the PAO, progressing systematically from west to east (Wang et al., 2019). These findings collectively support a scissor-like closure mechanism for the eastern PAO, characterized by initial closure in the western segment followed by progressive termination eastward (Zhang et al., 2016; Tang et al., 2018; Wang et al., 2019; Tian et al., 2020). In light of these constraints, we propose a tectonic subdivision of the SXCYS into two distinct segments for detailed analysis: (1) the eastern segment (Changchun–Yanji sector), and (2) the western segment (Solonker–Xar Moron River sector), to facilitate a more precise spatiotemporal investigation of the subduction–collision processes along the suture zone.

5.3.1 The evolution of the Changchun-Yanji section of the SXCYS

In the Changchun–Yanji segment of the SXCYS, the eastern Paleo-Asian Ocean (PAO) was characterized by a subduction-related tectonic regime from the Early Permian through to the Late Permian. Petrogenetic studies suggest that Early Permian tonalites and metamorphic dacites exposed along the northern margin of this segment were generated in an active continental margin setting (Yu et al., 2008; Wu et al., 2011), whereas coeval gabbros and basaltic andesites exhibit geochemical signatures diagnostic of a mature island arc environment (Cao et al., 2011; 2012). These findings provide evidence for the establishment of an active continental margin environment within a subduction system during the Early Permian, accompanied by the initiation of mature island arc magmatism. Notably, the absence of magmatic rock records

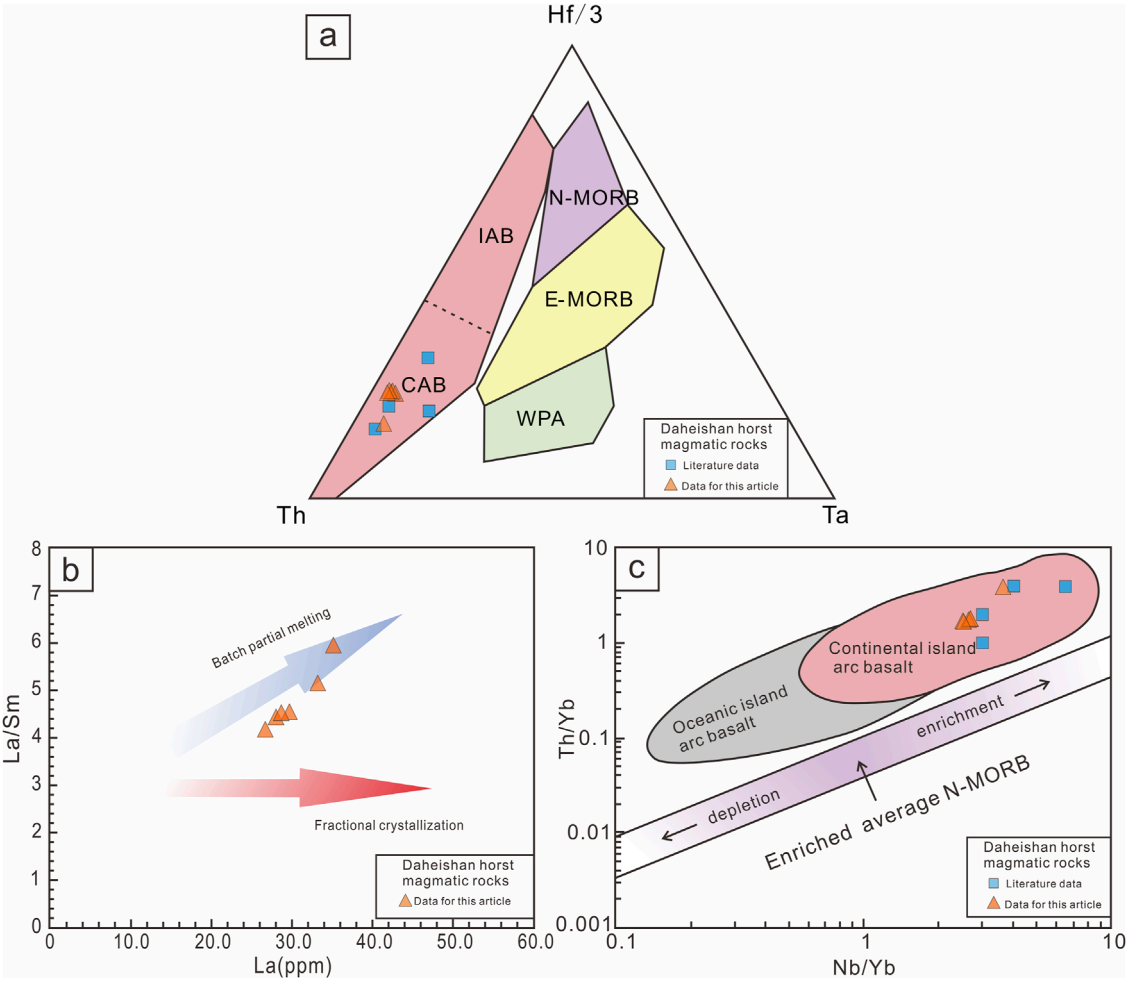

FIGURE 7
Tectonic discrimination diagrams for magmatic rocks. **(a)** Th-Ta-Hf/3 ternary diagram (after Wood et al., 1979); **(b)** La/Sm vs La diagram (after Allègre and Minster, 1978); **(c)** Nb/Yb vs Th/Yb diagram (after Pearce and Peate, 1995). The abbreviations shown in the figure are: IAB, Island Arc Tholeiitic Basalt Series; CAB, Calc-alkaline Basalt Series; WPA, Within-Plate Alkaline Basalt; N-MORB, Normal Mid-Ocean Ridge Basalt; E-MORB, Enriched Mid-Ocean Ridge Basalt. The literature data were cited from Han et al. (2017) and Song (2018).

in the Middle Permian reflects the weak magmatic activity in this period (Guan, 2018). Additionally, Late Permian intrusive rocks identified north of the Changchun-Yanji segment—including the Xinzhan gabbro-diorite (~256 Ma; Wang, 2016), the Xidahe diorite (~257 Ma; Wu et al., 2011), the Hunchun diorite (~255 Ma; Cao et al., 2011), and the dioritic porphyry dikes (~252.9 Ma) discovered in this study along the northern margin of the Daheishan Horst—are interpreted as products of northward subduction of the PAO beneath the Songliao–Xilinhot Block (Figure 8a). Additionally, the northern margin of the North China Block simultaneously entered a peak period of magmatic activity during the Permian (Zhang, 2021). A substantial volume of intermediate-acidic magmatic rocks and minor mafic rocks (293–252 Ma) have been identified across the region, formed under an active continental margin tectonic setting (Zhang and Zhu, 2000; 2004; Cao et al., 2011; Wu et al., 2011; Cao, 2013; Guan et al., 2016; Wang, 2016; Song et al., 2018). These lines of evidence support a model of continuous bidirectional subduction of the PAO in the Changchun–Yanji region during the Permian (293–252 Ma) (Figures 8a,b). Notably, Liu Y. J. et al. (2017) identified inherited zircons in Late Permian metamorphosed basalts from the Kaiyuan area and detrital zircons within marine strata of the Zhaobeishan Formation that were sourced from both the North China Craton and the Songliao-Xilinhot Block. This suggests that by the Late Permian, the two blocks were already in relatively close spatial proximity.

The Changchun–Yanji segment underwent a complete collisional and suturing process during the Late Permian to Triassic. Extensive east-west trending high-Mg andesite–diorite belts (252–240 Ma) identified within the accretionary orogen along the northern margin of the North China Craton (Li C. D. et al., 2007; Fu et al., 2010; Liu et al., 2012; Yuan et al., 2016; Shen et al., 2020) indicate a slab break-off event that occurred following the closure of the PAO. This suggests that a soft collision between the northeastern continental blocks and the northern margin of the North China Craton may have initiated as early as ~252 Ma. In

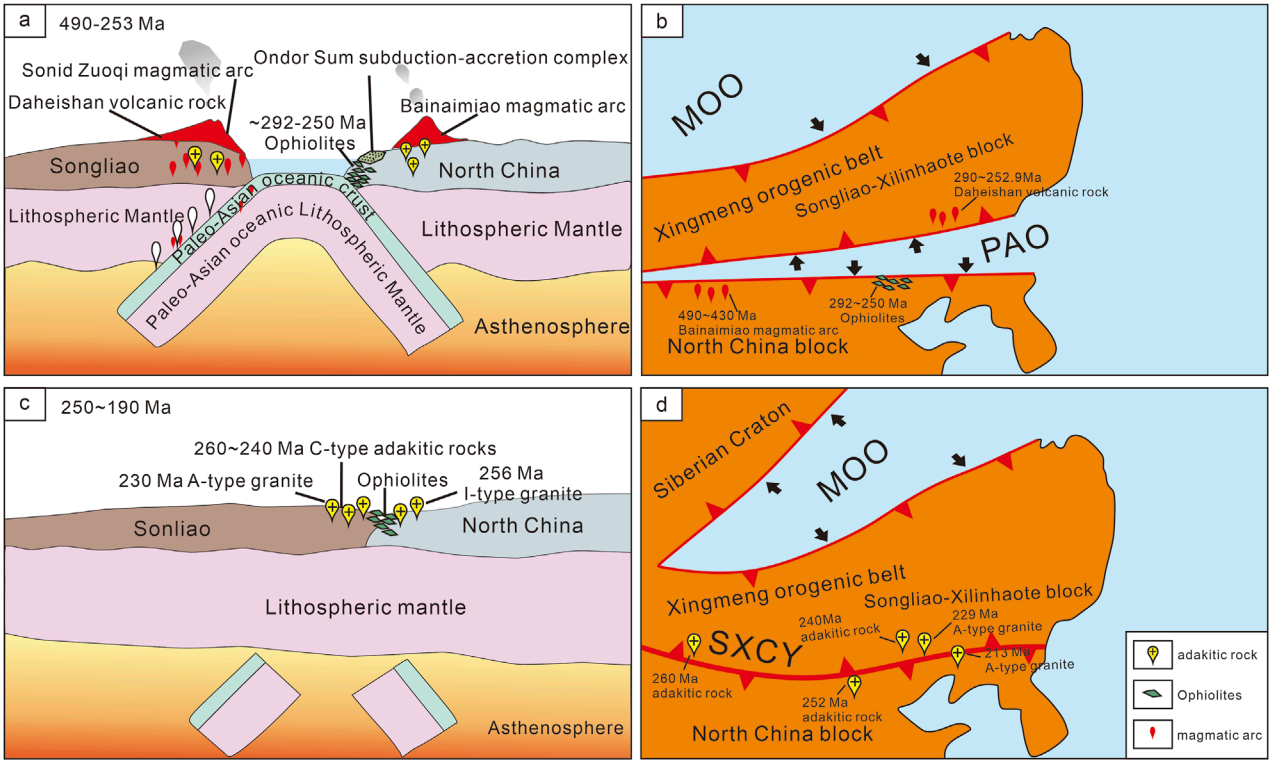

FIGURE 8
Tectonic evolution models of the eastern segment of the Paleo-Asian Ocean (PAO). **(a)** Tectonic model illustrating double-sided subduction of the eastern PAO; **(B and D)** Schematic diagrams illustrating scissor-style closure of the PAO (modified after Li, 2023); **(C)** Collisional closure tectonic model of the eastern PAO. The abbreviations shown in the figure are: PAO, Paleo-Asian Ocean; MOO, Mongol-Okhotsk Ocean; SXCY, Solonker-Xar Moron-Changchun-Yanji Suture Zone.

addition, Late Permian to Early–Middle Triassic (243.1–241.9 Ma) adakitic granitoids distributed linearly in central Jilin Province (Wu et al., 2021; Jing et al., 2023; Jing, 2023) further indicate sustained soft collision orogenic activity during the Middle Triassic (243.1–240 Ma). During the Late Triassic, the Changchun-Yanji suture zone witnessed widespread development of A-type granites (230–190 Ma), including the Dawanglazi, Qingshui, Maojiatun, Milin, and Tianqiaogang plutons (Wu et al., 2002; Sun et al., 2005), marking a transition into an extensional tectonic regime. Integrated analysis of coastal to terrestrial depositional systems (Xiao et al., 2009) combined with biological assemblage succession patterns (Wilde and Zhou, 2015) provides compelling evidence that the Changchun-Yanji suture zone had completed its collisional closure by the Late Triassic (~230 Ma), subsequently transitioning into a post-orogenic extensional phase (Figure 8c).

5.3.2 The evolution of the Solonker-Xar Moron section of the SXCYS

Previous studies have identified the Ulan Island Arc-Wenduermiao accretionary complex in central Inner Mongolia, south of the Solon-Xilamulun suture zone, which formed during southward subduction of the PAO in the Middle Ordovician to Early Silurian (467–429 Ma; Liu et al., 2019). North of the suture, a series of arc-related magmatic belts formed in response to northward subduction have been recognized, such as the Bainaimiao Arc (490–430 Ma; Xiao et al., 2003; Shi et al., 2005) and the Carboniferous magmatic arc in Sonid Zuoqi (350–310 Ma; Liu Y. J. et al., 2017). These findings collectively indicate that the eastern segment of the PAO was subject to sustained bidirectional (northward and southward) subduction prior to the Carboniferous. Critically, the Middle Permian Linxi Formation clastic rocks (~262.2 Ma) in Ar Horqin Banner (northern suture margin) record marine-continent transitional facies (Zhang et al., 2023). Concurrently, Middle Permian magmatism (269–260 Ma) in the Guyang-Huade area (southern suture margin) documents a magmatic shift from volcanic arc to syn-collisional granitoids (Gao, 2024). Moreover, Middle Permian radiolarian-conodont assemblages within the Xingshuwa ophiolitic mélange (Linxi area) confirm oceanic sedimentation (Wang and Fan, 1997). Collectively, these constraints demonstrate persistent subduction and oceanic basin existence through the Middle Permian, precluding final collision closure prior to this period.

Gao (2024) identified Late Permian (253–250 Ma) adakitic rocks with thickened lower-crustal signatures in the Guyang-Huade area of the Solonker-Xar Moron suture, exhibiting transitional features between syn-collisional and volcanic arc granitoids. This indicates the imminent closure of the Solonker-Xar Moron segment in this region during the terminal Permian. Significantly, coeval oceanic-type adakites at ~258.9 Ma (HFD1 borehole, northern Songliao

Basin; Zhang et al., 2024) constrain the collision onset timing. Furthermore, S-type granite (Dongshengmiao pluton, ~259 Ma; Wu et al., 2014), I-type granite (Siziwangqi, ~256 Ma; Liu et al., 2010), and S-type granite (Jiguanzi Mountain, ~245 Ma; Zhang et al., 2015) collectively demonstrate collision-related petrogenesis. These lines of evidence establish that: (1) The Solonker-Xar Moron segment initiated continent-continent collision at ~259 Ma, experiencing prolonged soft-collisional orogenesis until ~245 Ma; (2) In contrast, the Changchun-Yanji segment remained under ongoing oceanic subduction until ~252 Ma; (3) The eastern segment's initial collision (~252 Ma) postdated the western segment (~259 Ma).

Furthermore, syn-collisional granitoids (259–240 Ma) distributed along this suture zone display a systematic younging trend from west to east (Wang Z. W. et al., 2015). Moreover, the Shuangjingzi granite north of the Xar Moron River (~237 Ma; Li J. Y. et al., 2007) exhibits extensional features typical of post-orogenic tectonics, suggesting that the western segment entered a post-collisional extensional regime around ~237 Ma-earlier than the Changchun-Yanji segment, whose earliest post-collisional record is dated at ~230 Ma. Collectively, these data demonstrate that the main oceanic basin of the PAO closed progressively from west to east, exhibiting a "scissor-like" (diachronous) closure pattern.

In summary, the subduction-collision processes along the eastern segment of the PAO, represented by the SXCYS, exhibit pronounced temporal differences between its western and eastern segments. The closure occurred earlier in the west and later in the east, supporting a "scissor-like" (diachronous) closure model during the Late Permian to Early/Middle Triassic (Figures 8c,d). The youngest granitic rocks associated with collisional processes in the eastern segment are dated to the Middle Triassic (Wang Z. J. et al., 2015), which likely marks the final closure of the easternmost part of the PAO.

6 Conclusion

Zircon LA-ICP-MS U–Pb dating constrains the emplacement of the diorite porphyry from the Daheishan Horst to the Late Permian (252.9 ± 3.2 Ma, 1σ), overturning previous interpretations that suggested an Early to Middle Silurian metamorphic-magmatic origin. This age implies a unified Permian tectono-magmatic regime affecting both the northern and southern domains of the belt.

The diorite porphyry sample from the Daheishan Horst belongs to the medium-K calc-alkaline series. Geochemically, it exhibits marked enrichment in large ion lithophile elements (LILEs) and light rare earth elements (LREEs), coupled with pronounced depletion in high-field-strength elements (HFSEs; Nb, Ta, P, Ti). Depleted zircon Hf and whole-rock Sr–Nd isotopic signatures collectively demonstrate derivation from partial melting of a subduction-modified mantle source. These features are diagnostic of a subduction zone setting beneath an active continental margin.

The eastern segment of the Paleo-Asian Ocean (PAO) followed a bidirectional subduction and scissor-like closure model along the Solonker–Xar Moron–Changchun–Yanji suture zone (SXCYS), with oceanic closure progressing from west to east during the Late Permian to Early/Middle Triassic.

Data availability statement

The original contributions presented in the study are included in the article/supplementary material, further inquiries can be directed to the corresponding author.

Author contributions

JL: Writing – original draft, Writing – review and editing, Conceptualization, Data curation, Formal Analysis, Investigation, Methodology, Software, Project administration, Supervision. QW: Writing – original draft, Writing – review and editing, Conceptualization, Data curation, Investigation, Methodology, Software, Supervision. ML: Data curation, Writing – original draft, Writing – review and editing, Methodology, Supervision, Validation, Visualization. SJ: Writing – original draft, Writing – review and editing, Formal Analysis, Investigation, Resources, Software. JH: Formal Analysis, Investigation, Software, Writing – original draft, Writing – review and editing, Resources. LG: Writing – original draft, Writing – review and editing, Formal Analysis, Investigation, Methodology, Resources, Software. YY: Writing – original draft, Writing – review and editing, Formal Analysis, Investigation, Resources, Software. HY: Conceptualization, Data curation, Formal Analysis, Investigation, Software, Supervision, Writing – original draft, Writing – review and editing, Resources.

Funding

The author(s) declare that no financial support was received for the research and/or publication of this article.

Conflict of interest

Authors JL, ML, SJ, and JH were employed by PetroChina Daqing Oilfield Company Limited.

The remaining authors declare that the research was conducted in the absence of any commercial or financial relationships that could be construed as a potential conflict of interest.

Generative AI statement

The author(s) declare that no Generative AI was used in the creation of this manuscript.

Any alternative text (alt text) provided alongside figures in this article has been generated by Frontiers with the support of artificial intelligence and reasonable efforts have been made to ensure accuracy, including review by the authors wherever possible. If you identify any issues, please contact us.

Publisher's note

References

Allègre, C. J., and Minster, J. F. (1978). Quantitative models of trace element behavior in magmatic processes. *Earth Planet Sci. Lett.* 38, 1–25. doi:10.1016/0012-821x(78)90123-1

Andersen, T. (2002). Correction of common lead in u–pb analyses that do not report 204pb. *Chem. Geol.* 192, 59–79. doi:10.1016/s0009-2541(02)00195-x

Blichert-Toft, J., Chauvel, C., and De, F. (1997). Separation of hf and lu for high-precision isotope analysis of rock samples by magnetic sector-multiple collector icp-ms. *Contributions Mineral. Petrol.* 127 (3), 248–260.

Cao, H. H. (2013). Geochronology and geochemistry of late paleozoic-early Mesozoic igneous rocks in the eastern part of the northern margin of the North China plate. Doctoral dissertation. Changchun: Jilin University. (in Chinese with English abstract).

Cao, H. H., Xu, W. L., Pei, F. P., Wang, Z. W., Wang, F., and Wang, Z. J. (2011). Permian tectonic evolution in southwestern khanka massif: evidence from zircon U-Pb chronology, hf isotope and geochemistry of gabbro and diorite. *Acta Geol. Sin. - Engl. Ed.* 85, 1390–1402. doi:10.1111/j.1755-6724.2011.00594.x

Cao, H. H., Xu, W. L., Pei, F. P., Guo, P. Y., and Wang, F. (2012). Permian tectonic attributes of the eastern section of the northern margin of the North China plate: constraints from volcanic zircon U-Pb geochronology and geochemistry. *Acta Petrol Sin.* 28, 2733–2750. (in Chinese with English abstract).

Cao, H. H., Xu, W. L., Pei, F. P., Wang, Z. W., Wang, F., and Wang, Z. J. (2013). Zircon u–pb geochronology and petrogenesis of the late paleozoic–early mesozoic intrusive rocks in the eastern segment of the northern margin of the north China block. *Lithos* 170-171, 191–207. doi:10.1016/j.lithos.2013.03.006

Eizenhöfer, P. R., Zhao, G., Zhang, J., and Sun, M. (2014). Final closure of the paleo-asian ocean along the solonker suture zone: constraints from geochronological and geochemical data of permian volcanic and sedimentary rocks. *Tectonics* 33, 441–463. doi:10.1002/2013tc003357

Fisher, C. M., Vervoort, J. D., and Hanchar, J. M. (2014). Guidelines for reporting zircon hf isotopic data by la-mc-icpms and potential pitfalls in the interpretation of these data. *Chem. Geol.* 363, 125–133. doi:10.1016/j.chemgeo.2013.10.019

Fu, C. L., Sun, D. Y., Zhang, X. Z., Wei, H. Y., and Gou, J. (2010). Discovery and geological significance of Triassic high-Mg diorite in Hunchun, Jilin Province. *Acta Petrol Sin.* 26, 1089–1102. (in Chinese with English abstract).

Gao, Y. G. (1985). Daheishan conglomerate and its geological significance. *Jilin Geol.* 2 (02), 53–59+85. (in Chinese with English abstract).

Gao, J. H. (2024). Late Paleozoic magmatism and sedimentation in the middle section of the northern margin of the North China Craton (Guyang-Huade)and its geodynamic significance. Doctoral dissertation. Changchun: Jilin University. (in Chinese with English abstract).

Guan, Q. B. (2018). Permian-early Jurassic tectonic evolution of the Kaiyuan-Yanji area in the eastern part of the northern margin of the North China plate D. Doctoral dissertation. Changchun: Jilin University. (in Chinese with English abstract).

Guan, Q. B., Li, S. C., Zhang, C., Shi, Y., and Li, P. C. (2016). Zircon U-Pb dating, geochemical characteristics and geological significance of i-type granites in the eastern section of the southern margin of the Xingmeng orogenic belt and Helong area. *Acta Petrol Sin.* 32, 2690–2706. (in Chinese with English abstract).

Han, Z. Z., Song, Z. G., Gao, L. H., Han, M., Guo, Z. P., Zhong, W. J., et al. (2017). Late Paleozoic volcanic events and their tectonic significance in the "Daheishan horst belt" of Jilin province. *Geol. Front.* 24 (2), 186–201. (in Chinese with English abstract). doi:10.13745/j.esf.2017.02.018

Hu, Z., Gao, S., Liu, Y., Hu, S., Chen, H., and Yuan, H. (2008a). Signal enhancement in laser ablation icp-ms by addition of nitrogen in the central channel gas. *J. Anal. Atomic Spectrom.* 23 (8), 1093–1101. doi:10.1039/b804760j

Hu, Z. C., Liu, Y. S., Gao, S., Hu, S. H., Dietiker, R., and ang Günther, D. (2008b). A local aerosol extraction strategy for the determination of the aerosol composition in laser ablation inductively coupled plasma mass spectrometry. *J. Anal. Atomic Spectrom.* 23 (9), 1192–1203. doi:10.1039/b803934h

Hu, Z., Liu, Y., Gao, S., Xiao, S., Zhao, L., Günther, D., et al. (2012a). A "wire" signal smoothing device for laser ablation inductively coupled plasma mass spectrometry analysis. *Spectrochim. Acta Part B At. Spectrosc.* 78, 50–57. doi:10.1016/j.sab.2012.09.007

Hu, Z. C., Liu, Y. S., Gao, S., Liu, W. G., Zhang, W., Tong, X. R., et al. (2012b). Improved *in situ* hf isotope ratio analysis of zircon using newly designed x skimmer cone and jet sample cone in combination with the addition of nitrogen by laser ablation multiple collector icp-ms. *J. Anal. Atomic Spectrom.* 27, 1391. doi:10.1039/c2ja30078h

Jackson, S. E., Pearson, N. J., Griffin, W. L., and Belousova, E. A. (2004). The application of laser ablation-inductively coupled plasma-mass spectrometry to *in situ* u–pb zircon geochronology. *Chem. Geol.* 211, 47–69. doi:10.1016/j.chemgeo.2004.06.017

Jia, D. C. (1990). Early Paleozoic magmatic evolution characteristics and its relationship with minerals in Fangniugou area, Yitong county. *Jilin Geol.* 9 (2), 49–56. (in Chinese with English abstract).

Jiang, Z. L. (2014). Early paleozoic lithofacies palaeogeography of the Xingmeng-Jihei orogenic Belt in Northeast China: early Paleozoic lithofacies palaeogeography of the Xingmeng-Jihei orogenic Belt in Northeast China. *Pet. Ind. Publ. House*. (in Chinese with English abstract).

Jing, Y. (2023). Late Paleozoic-early mesozoic magmatism and deep geodynamic process in northern Liaoning. *Jilin Univ.* 135, 3128–3142.

Jing, Y., Ji, Z., Ge, W. C., Dong, Y., Yang, H., and Bi, J. H. (2021). Middle–late permian i-type granitoids from the diaobingshan region in the northern margin of the north China craton: insight into southward subduction of the paleo–asian ocean. *Int. Geol. Rev.* 63, 357–379. doi:10.1080/00206814.2020.1712556

Jing, Y., Ge, W. C., Yang, H., Dong, Y., Ji, Z., Bi, J. H., et al. (2023). High-magnesium igneous associations record final-stage geodynamic process of the southeastern segment of the central Asian orogenic belt. *Gsa Bull.* 135, 3128–3142. doi:10.1130/b36472.1

Li, J. Y. (2006). Permian geodynamic setting of northeast China and adjacent regions: closure of the paleo-asian ocean and subduction of the paleo-pacific plate. *J. Asian Earth Sci.* 26, 207–224. doi:10.1016/j.jseaes.2005.09.001

Li, E. Z., (2012). Seismicity of Yitong-Shulan fault zone (Changchun section) and its influence on urban development of Changchun. Doctoral dissertation. Changchun: Jilin University. (in Chinese with English abstract).

Li, M. Q. (2023). The Permian-Mesozoic tectonic evolution of the Jizhong area in the eastern part of the northern margin of the North China plate. Doctoral dissertation. Changchun: Jilin University. (in Chinese with English abstract).

Li, C. D., Zhang, F. Q., Miao, L. C., Jie, H. Q., and Xu, Y. W. (2007a). Zircon chronology and geochemical characteristics of late Permian high-Mg andesite shrimp in Seluohe, Jilin province. *Acta Petrol Sin.* 23, 767–776. (in Chinese with English abstract).

Li, J. Y., Gao, L. M., Sun, G. H., Li, Y. P., and Wang, Y. B. (2007b). The determination of the Middle Triassic syn-collisional crust-derived granite in Shuangjingzi, eastern Inner Mongolia and its constraint on the collision time limit between Siberia and Sino-Korean ancient plates. *Acta Petrol. Sin.* (03), 565–582. (in Chinese with English abstract).

Liu, C. F., Zhang, H. R., Yu, Y. S., Zhou, Z. G., Liu, W. C., and Zhang, H. F. (2010). Zircon U-Pb dating and petrochemistry of the arctic intrusions in the Siziwangqi area, central Inner Mongolia. *Mod. Geol.* 24 (1), 112–119. (in Chinese with English abstract). doi:10.1016/j.lithos.2009.10.009

Liu, Y. S., Gao, S., Hu, Z. C. H., Gao, C. G., Zong, K. Q., and Wang, D. B. (2010a). Continental and Oceanic crust recycling-induced melt–peridotite interactions in the trans-North China orogen: U–Pb dating, Hf isotopes and trace elements in zircons from Mantle xenoliths. *J. Petrology* (1-2), 392–399. doi:10.1093/petrology/egp082

Liu, Y. S., Gao, S., Hu, Z. C., Gao, C. G., Zong, K. Q., and Wang, D. B. (2010b). Continental and oceanic crust recycling-induced melt–peridotite interactions in the trans-north China orogen: u–pb dating, hf isotopes and trace elements in zircons from mantle xenoliths. *J. Petrol* 51, 537–571. doi:10.1093/petrology/egp082

Liu, Y. S., Wang, X. H., Wang, D. B., He, D. T., Zong, K. Q., Gao, C., et al. (2012). Triassic high-mg adakitic andesites from Linxi, inner Mongolia: insights into the fate of the paleo-asian ocean crust and fossil slab-derived melt–peridotite interaction. *Chem. Geol.* 328, 89–108. doi:10.1016/j.chemgeo.2012.03.019

Liu, H., Guo, H., Xing, L., Zhan, Y., Li, F., Shao, J., et al. (2016). Geochemical behaviors of rare earth elements in groundwater along a flow path in the North China Plain. *J. Asian Earth Sci.* 117, 33–51. doi:10.1016/j.jseaes.2015.11.021

Liu, J., Liu, Z. H., Zhao, C., Wang, C. J., Guan, Q. B., Dou, S. Y., et al. (2017). Geochemistry and u–pb detrital zircon ages of late permian to early triassic metamorphic rocks from northern Liaoning, North China: evidence for the timing of final closure of the paleo-asian ocean. *J. Asian Earth Sci.* 145, 460–474. doi:10.1016/j.jseaes.2017.06.026

Liu, Y. J., Li, W. M., Feng, Z. Q., Wen, Q. B., Neubauer, F., and Liang, C. Y. (2017). A review of the paleozoic tectonics in the eastern part of central Asian orogenic belt. *Gondwana Res.* 43, 123–148. doi:10.1016/j.gr.2016.03.013

Liu, Y. J., Feng, Z. Q., Jiang, L. W., Jin, W., Li, W. M., Guan, Q. B., et al. (2019). Ophiolites in Northeast China. *Acta Petrol Sin.* 35, 3017–3047. (in Chinese with English abstract).

Middlemost, E. A. K. (1994). Naming materials in the magma/igneous rock system. *Earth Sci. Rev.* 37, 215–224. doi:10.1016/0012-8252(94)90029-9

Mou, R. T. (2022). Geochronology, geochemistry and tectonic significance of early Permian volcanic rocks in Yitong area, Jilin Province. Doctoral dissertation. Changchun: Jilin University. (in Chinese with English abstract).

Pearce, J. A. (1982). Trace element characteristics of lavas from destructive plate boundaries. *Andesites*, 525–548.

Pearce, J. A., and Peate, D. W. (1995). Tectonic implications of the composition of volcanic arc magmas. *Annu. Rev. Earth Planet Sci.* 23, 251–285. doi:10.1146/annurev.earth.23.1.251

Peng, Y. J., Li, D. J., and Xie, Z. (1979). The discovery of the early Silurian graptolite-shale facies strata in Taoshan, Yitong county, Jilin Province and its geological significance. *Regional Geol. Jilin* 3 (1), 1–15. (in Chinese with English abstract).

Qiu, L., Fu, Y., Yan, D. P., Wang, T. H., Gan, W., Li, C. M., et al. (2024). Timing, geometry, and kinematics of the Yilan-Yitong fault zone in the northern tan-lu fault system of northeast Asia. *China Geol.* 8 (2), 265–280. doi:10.31035/cg20230060

Ren, Q., Zhang, S., Gao, Y., Zhao, H., Wu, H., Yang, T., et al. (2020). New middle–late permian paleomagnetic and geochronological results from inner Mongolia and their paleogeographic implications. *J. Geophys. Res. Solid Earth* 125, e2019JB019114. doi:10.1029/2019jb019114

Rickwood, P. C. (1989). Boundary lines within petrologic diagrams which use oxides of major and minor elements. *Lithos* 22, 247–263. doi:10.1016/0024-4937(89)90028-5

Shen, Y. J., Chen, B., Li, J. Y., Sun, J. L., Zhao, C. J., Zheng, T., et al. (2020). Geochemical characteristics, petrogenesis and geological significance of early triassic high-Mg diorite in central Jilin. *J. Heilongjiang Univ. Sci. Technol.* 30 (5), 481–489+531.

Shi, Y. R., Liu, D. Y., Jian, P., Zhang, F. Q., Miao, L. C., Shi, G. H., et al. (2005). The petrogenesis and shrimp dating of the baiyinbaolidao adakitic rocks in southern Suzuoqi, inner Mongolia. *Acta Petrol. Sin.* 21, 143–150.

Shi, C. L., Ding, X. Z., Liu, Y., X. Zhou, X. D., and Nie, L. J. (2020). Zircon u–pb geochronology and petrogenesis of early–midlle permian arc–related volcanic rocks in central Jilin: implications for the tectonic evolution of the eastern segment of central Asian orogenic belt. *Acta Geol. Sin. - Engl. Ed.* 94, 1207–1222. doi:10.1111/1755-6724.14568

Song, Z. G. (2018). *Genesis and geological significance of late Permian magmatic rocks in Jingtai-Leshan area, Jilin Province.* (doctoral dissertation). Shandong University of Science and Technology, Qingdao, China.

Song, Z. G., Han, Z. Z., Gao, L. H., Geng, H. Y., Li, X. P., Meng, F. X., et al. (2018). Permo-triassic evolution of the southern margin of the central Asian orogenic belt revisited: insights from late permian igneous suite in the Daheishan horst, ne China. *Gondwana Res.* 56, 23–50. doi:10.1016/j.gr.2017.12.005

Sun, S. S., and McDonough, W. F. (1989). Chemical and isotopic systematics of oceanic basalts: implications for mantle composition and processes. *Geol. Soc. Lond. Special Publ.* 42 (1), 313–345. doi:10.1144/gsl.sp.1989.042.01.19

Sun, D. Y., Wu, F. Y., Gao, S., and Lu, X. P. (2005). Confirmation of two episodes of a-type granite emplacement during late Triassic and early Jurassic in the central Jilin province, and their constraints on the structural pattern of eastern Jilin-Heilongjiang area, China. *Earth Sci. Front.* 12, 263–275. (in Chinese with English abstract).

Sun, S. Q., Zhang, C. J., and Zhao, S. J. (2007). Discrimination of trace elements in continental intraplate tectonic environment. *Geotect. Metallogeny* (01), 104–109. doi:10.16539/j.ddgzyckx.2007.01.012

Tang, J., Xu, W. L., Wang, F., and Ge, W. C. (2018). Subduction history of the paleo-pacific slab beneath Eurasian continent: mesozoic-paleogene magmatic records in northeast Asia. *Sci. China Earth Sci.* 61, 527–559. doi:10.1007/s11430-017-9174-1

Tian, R., Xie, G., Zhu, W., Zhang, J., Gao, S., Zhang, B., et al. (2020). Late Paleozoic tectonic evolution of the Paleo - Asian Ocean in the northern Alxa Block (NW China). *Tectonics* 39, e2020TC006359. doi:10.1029/2020tc006359

Wang, Z. J. (2016). Late Paleozoic-Triassic tectonic evolution of the eastern section of the southern margin of the Xing-Meng orogenic belt:evidence from detrital zircon U-Pb geochronology and igneous rock assemblages. Doctoral dissertation. Changchun: Jilin University. (in Chinese with English abstract).

Wang, Y. J., and Fan, Z. Y. (1997). Discovery and geological significance of permian radiolarians in the ophiolite belt of northern Xilamulun River, Inner Mongolia. *Acta Palaeontol. Sin.* 36 (1), 58–69. (in Chinese with English abstract). doi:10.19800/j.cnki.aps.1997.01.005

Wang, Y. Q., and Su, Y. Z. (1996). Regional stratigraphic development and crustal evolution in Northeast China. *Jilin Geol.* (Z1), 118–133+1. (in Chinese with English abstract).

Wang, Z. J., Xu, W. L., Pei, F. P., Wang, Z. W., Li, Y., and Cao, H. H. (2015a). Geochronology and geochemistry of middle permian–middle triassic intrusive rocks from central–eastern Jilin province, ne China: constraints on the tectonic evolution of the eastern segment of the paleo-asian ocean. *Lithos* 238, 13–25. doi:10.1016/j.lithos.2015.09.019

Wang, Z. W., Pei, F. P., Xu, W. L., Cao, H. H., and Wang, Z. J. (2015b). Geochronology and geochemistry of late devonian and early carboniferous igneous rocks of central Jilin province, ne China: implications for the tectonic evolution of the eastern central asian orogenic belt. *J. Asian Earth Sci.* 97, 260–278. doi:10.1016/j.jseaes.2014.06.028

Wang, X., Ren, Y. S., Zhang, Y., and Zhao, D. S. (2019). Sedimentary response to the non-synchronous closure of Paleo-asian ocean: evidence from u-pb ages and hf isotopic compositions of detrital zircons from the linxi formation, ne China. *Int. Geol. Rev.* 63, 144–160. doi:10.1080/00206814.2019.1706650

Wilde, S. A., and Zhou, J. B. (2015). The late paleozoic to mesozoic evolution of the eastern margin of the central asian orogenic belt in China. *J. Asian Earth Sci.* 113, 909–921. doi:10.1016/j.jseaes.2015.05.005

Wood, D. A. (1980). The application of a thhfta diagram to problems of tectonomagmatic classification and to establishing the nature of crustal contamination of basaltic lavas of the British tertiary volcanic province. *Earth Planet Sci. Lett.* 50, 11–30. doi:10.1016/0012-821x(80)90116-8

Wood, D. A., Joron, J. L., and Treuil, M. A. (1979). A re-appraisal of the use of trace elements to classify and discriminate between magma series erupted in different tectonic settings. *Earth Planet Sci. Lett.* 45, 326–336. doi:10.1016/0012-821x(79)90133-x

Wu, S. B. (1994). Early Paleozoic strata in Jilin trough area. *Jilin Geol.* (01), 1–9+23. (in Chinese with English abstract).

Wu, F. Y., Sun, D. Y., Li, H. M., Jahn, B., and Wilde, S. A. (2002). A-type granites in northeastern China: age and geochemical constraints on their petrogenesis. *Chem. Geol.* 187, 143–173. doi:10.1016/s0009-2541(02)00018-9

Wu, F. Y., Sun, D. Y., Ge, W. C., Zhang, Y., Grant, M. L., Wilde, S. A., et al. (2011). Geochronology of the phanerozoic granitoids in northeastern China. *J. Asian Earth Sci.* 41, 1–30. doi:10.1016/j.jseaes.2010.11.014

Wu, Y. F., Wang, X. L., Zeng, J. N., Cao, J. J., Lu, S. F., and Sun, X. D. (2014). Geochemical characteristics and tectonic significance of the Dongshengmiao pluton in the western section of the northern margin of the North China plate. *Mineral. rock Geochem. Bull.* 33 (06), 820–829. (in Chinese with English abstract).

Wu, D. D., Li, S., Chew, D., Liu, T. Y., and Guo, D. H. (2021). Restriction of the Permian-Triassic granitic magma evolution on the accretion-collision process in the southeastern margin of the Central Asian orogenic belt. *Chin. Sci. Earth Sci.* 51, 906–926. (in Chinese with English abstract).

Xiao, W. J., Windley, B. F., Hao, J., and Zhai, M. G. (2003). Accretion leading to collision and the permian solonker suture, inner Mongolia, China: termination of the central asian orogenic belt. *Tectonics* 22. doi:10.1029/2002tc001484

Xiao, W. J., Kröner, A., and Windley, B. (2009). Geodynamic evolution of central Asia in the paleozoic and mesozoic. *Int. J. Earth Sci.* 98, 1185–1188. doi:10.1007/s00531-009-0418-4

Yang, J. H., Wu, F. Y., Shao, J. A., Wilde, S. A., and Liu, X. M. (2007). Constraints on the timing of uplift of the Yanshan fold and thrust belt, North China. *Earth Planet. Sci. Lett.* 246 (3-4), 336–352. doi:10.1016/j.epsl.2006.04.029

Yu, J. J., Men, L. J., Chen, L., Zhao, J. K., Liang, S. N., Chen, D., et al. (2008). Zircon SHRIMP U-Pb ages of metamorphic dacites from the Wudaogou Group in Yanbian area and their geological significance. *J. Jilin Univ. Sci. Ed.* 38 (3), 363–0367. (in Chinese with English abstract).

Yu, Q., Ge, W. C., Yang, H., Zhao, G. C., Zhang, Y. L., and Su, L. (2014). Petrogenesis of late paleozoic volcanic rocks from the Daheshen formation in central Jilin province, ne China, and its tectonic implications: constraints from geochronology, geochemistry and sr–nd–hf isotopes. *Lithos* 192-195, 116–131. doi:10.1016/j.lithos.2014.01.016

Yuan, L. L., Zhang, X. H., Xue, F. H., Lu, Y. H., and Zong, K. Q. (2016). Late permian high-mg andesite and basalt association from northern Liaoning, North China: insights into the final closure of the paleo-asian ocean and the orogen–craton boundary. *Lithos* 258-259, 58–76. doi:10.1016/j.lithos.2016.04.024

Zhang, L. (2021). Late Paleozoic tectonic evolution of the eastern segment of the northern margin of the North China Plate. Doctoral dissertation. Changchun: Jilin University. (in Chinese with English abstract).

Zhang, Z. C. (2024). Is the La/Sm-La diagram used to determine whether magmatic rocks are formed by fractional crystallization or partial melting. *Mod. Geol.* 38 (02), 547–548. (in Chinese with English abstract).

Zhang, J. F., and Zhu, H. C. (2000). Genetic types and tectonic setting of granites in Yanbian area. *Liaoning Geol.* 17 (1), 25–33. (in Chinese with English abstract).

Zhang, Y. B., Wu, F. Y., Wilde, S. A., Zhai, M. G., Lu, X. P., and Sun, D. Y. (2004). Zircon u–pb ages and tectonic implications of 'early paleozoic' granitoids at Yanbian, Jilin province, Northeast China. *Isl. Arc* 13, 484–505. doi:10.1111/j.1440-1738.2004.00442.x

Zhang, J. Z., Sun, G. S., Qu, Y. X., Sun, Z. J., Su, R., Li, X. P., et al. (2015). Geochemical characteristics and tectonic setting of Jiguanzishan monzonitic granite in Aohan Banner, Inner Mongolia. *World Geol.* 34, 345–353. (in Chinese with English abstract).

Zhang, S. H., Zhao, Y., Liu, J. M., and Hu, Z. C. (2016). Different sources involved in generation of continental arc volcanism: the Carboniferous–Permian volcanic rocks in the northern margin of the North China block. *Lithos* 240-243, 382–401. doi:10.1016/j.lithos.2015.11.027

Zhang, D., Huang, B., Zhao, G., Meert, J. G., Williams, S., Zhao, J., et al. (2021). Quantifying the extent of the paleo-asian ocean during the late carboniferous to early permian. *Geophys Res. Lett.* 48, e2021GL094498. doi:10.1029/2021gl094498

Zhang, H., Zhang, H., Shen, S., Zhao, Z., Qiu, L., Chen, S., et al. (2023). Volcanic age and geochemistry of the Permian Linxi formation in northeast China: implications for the tectonic evolution of the paleo-asian ocean. *Lithosphere* 2023 (1), lithosphere_2023_192. doi:10.2113/2023/lithosphere_2023_192

Zhang, H., Qiu, L., Zhang, J., Ma, Y., Zhang, Y., Chen, S., et al. (2024). Discovery of late Permian adakite in Eastern Central Asian orogenic Belt: implications for tectonic evolution of Paleo-Asian Ocean. *Minerals* 14, 386. doi:10.3390/min14040386

Zhao, C. J. (1996). *Tectonic framework and tectonic evolution of eastern Jilin-Heilongjiang*. Shenyang: Liaoning University Press.

Zhou, J. B., Wilde, S. A., Zhang, X. Z., Zhao, G. C., Liu, F. L., Qiao, D. W., et al. (2011). A >1300km late Pan-African metamorphic belt in ne China: new evidence from the Xing'an block and its tectonic implications. *Tectonophysics* 509, 280–292. doi:10.1016/j.tecto.2011.06.018